Sequential Estimation of Fixed-Wing UAV Aerodynamic Coefficients: Evaluation on Pitch/Roll Flight Data

A. Kempf[a, b], E. Roussel[a], G. Strub[a], J. Farnault[a], D. Delmas[a] and E. Laroche[b]
[a]French-German Research Institute of Saint-Louis, France
E-mail: {aurelie.kempf, emmanuel.roussel, guillaume.strub}@isl.eu
[b]University of Strasbourg, France
E-mail: laroche@unistra.fr

ABSTRACT

This paper presents a nonlinear system identification method for fixed-wing Unmanned Aerial Vehicles (UAVs) and its application to the estimation of aerodynamic coefficient derivatives of a Vertical Take-Off and Landing (VTOL) drone. The approach relies on a physics-based nonlinear model of the system and requires only a few dozen seconds of flight dataset, thereby minimizing the experimental burden. The identification process is based on the output-error method, applied sequentially to several sub-models. Hence, the aerodynamic coefficients are estimated in stages, which eliminates strong parameter interdependence and enhances model identifiability. The results obtained on the VTOL prototype are consistent with coefficient values predicted from Computational Fluid Dynamics simulations, and provide a satisfactory fit to the flight data. The methodology is generic and can be applied to other nonlinear aerial systems.

1 INTRODUCTION

Systems such as Vertical Take Off and Landing (VTOL) aircraft have attracted increasing interest over the last two decades, but come with complex aerodynamic behavior [1, 2]. Consequently, a controller that can handle wide-ranging changes in the whole flight envelope is needed. Designing such a controller requires an accurate aerodynamic model.

While Computational Fluid Dynamics (CFD) simulations and wind tunnel tests can provide high-fidelity estimations of the steady-state aerodynamic coefficients [3, 4], these methods are expensive and time-consuming. Moreover, estimating dynamic coefficients requires unsteady flow conditions impractical for typical wind tunnel setups, or coupled CFD/dynamics that are often computationally prohibitive. System identification from flight tests provides an efficient data-driven alternative to estimate the aerodynamic coefficients [5, 6, 7, 8]. Existing system identification approaches can broadly be categorized into neural-network-based, frequency-domain, and time-domain methods. Artificial neural networks are attractive when first-principles models are difficult to obtain [9]. Although effective for capturing complex nonlinear UAV dynamics, they produce black-box models with limited physical interpretability. System identification can also be performed in the frequency domain, using methods such as output-error, equation error or empirical transfer function estimate [10]. These methods are generally computationally efficient, although the transformation from time to frequency domain may result in information loss. In the time domain, recursive parameter estimation techniques enable online estimation using algorithms such as recursive least squares, recursive output-error and augmented Kalman filtering. These recursive methods are well suited for time-varying parameter tracking. Nevertheless, their slower convergence and potentially lower final accuracy make offline methods preferable for high-precision model development. For instance, filter-error methods, which typically rely on Kalman filtering [11], account for both process and measurement noise, but require higher computational cost. Equation error methods rely on least-squares estimation, which consists in minimizing a cost function defined in terms of an input-output equation [12]. Recent advances include sparse identification methods (SINDy), which use L1-regularized regression on candidate function libraries to automatically discover parsimonious nonlinear models from measured states [13]. These techniques are appreciated for their mathematical simplicity. However, all the system states and their time derivatives need to be measured, which is not always possible. Finally, the output-error method minimizes prediction errors between measured and simulated outputs obtained from model integration. It can handle nonlinear systems of arbitrary complexity, although they typically model uncertainty only through measurement noise.

Unlike traditional approaches that separate only longitudinal and lateral-directional dynamics [10, 11, 12], a method that estimates aerodynamic derivatives using more steps is proposed in [14]. This approach involves four steps: 1/ an initial polynomial fit for lift, drag, and moment coefficients and identification of longitudinal model; 2/ identification of lateral model; 3/ combined estimation of remaining coefficients; 4/ a final simultaneous adjustment of all derivatives. To obtain their results, the authors have performed about 400 maneuvers. In contrast, this paper presents a similar physics-based nonlinear identification method applied to a simpler model, enabling to use fewer datasets. It achieves satisfactory results for a VTOL UAV in fixed-wing mode by sequentially applying the output-error method to seven decoupled submodels.

The remaining sections of this article are organized as follows. Section 2 provides an overview of the VTOL drone that is used in this study. Then, Section 3 details the system modeling, and Section 4 derives the nonlinear identification method. Finally, Section 5 concludes the paper.

2 SYSTEM OVERVIEW

The proposed identification method has been evaluated on the VTOL tail-sitter UAV that is presented in Figure 1. It has four control surfaces at the wing's trailing edge; two are operating as elevons and two as rudderons. They are controlled using three servomotors (two for the elevons, one for the rudder). The UAV is powered by a single engine located in the middle of the wing. The powertrain is composed of a Hacker A30-16M Brushless DC motor, an APC 8×8E propeller and a Dualsky Summit 60X U8 Electronic Speed Controller (ESC). The avionics are centered around a mRO Control Zero H7 Pixhawk-compatible autopilot running PX4 [15]. Besides the IMU and barometer onboard the autopilot, a Pitot tube is fitted in the front of the aircraft. The airframe is constructed of extruded polystyrene stock with carbon/glass fiber reinforcement at the leading edge. During collection of identification data, the UAV is piloted by remote control, and monitored through a telemetry link to a ground station.

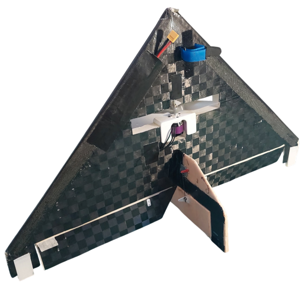

Figure 1: VTOL tail-sitter UAV.

3 SYSTEM MODELING

A standard approach is described with notations taken from [16]. In this paper, the roundness of the Earth is neglected, as well as its rotational speed; the ground-related coordinate system is inertial; the UAV is a rigid body.

3.1 Notations and Coordinate Systems

1. *Inertial Frame $\mathcal{F}^i$:* The i^i-axis is oriented toward north, the j^i-axis toward east, and the k^i-axis is directed toward the Earth's center.

2. *Body Frame $\mathcal{F}^b$:* The body frame is fixed to the aircraft and is used to describe its position and orientation. Its origin is located at the UAV's center of mass. Its axes (i^b, j^b, k^b) are oriented forward, to the right wing, and downward, respectively. The orientation of the body with respect to the inertial frame is described by the Euler angles (roll ϕ, pitch θ, yaw ψ), defined by the aerospace-standard ZYX rotation sequence.

3. *Wind Frame $\mathcal{F}^w$:* It is aligned with the direction of the airflow relative to the aircraft. Its origin is situated at the UAV's center of mass, and is defined by the axes (i^w, j^w, k^w). By definition, the relative airspeed vector lies along the i^w-axis.

To describe the equations of motion of the UAV, twelve state variables are used and described in Table 1.

Sym.	Description
p_n	Position along the i^i axis in $\mathcal{F}^i$
p_e	Position along the j^i axis in $\mathcal{F}^i$
p_d	Position along the k^i axis in $\mathcal{F}^i$
u	Velocity along the i^b axis in $\mathcal{F}^b$
v	Velocity along the j^b axis in $\mathcal{F}^b$
w	Velocity along the k^b axis in $\mathcal{F}^b$
ϕ	Roll angle
θ	Pitch angle
ψ	Yaw angle
p	Angular velocity about the i^b axis in $\mathcal{F}^b$
q	Angular velocity about the j^b axis in $\mathcal{F}^b$
r	Angular velocity about the k^b axis in $\mathcal{F}^b$

Table 1: State vector for the equations of motion

3.2 Flight Dynamics

Let $\boldsymbol{a}^b_{BE}$, $\boldsymbol{v}^b_{BE}$, $\boldsymbol{\omega}^b_{BE}$ respectively be the acceleration, the velocity and the angular velocity of the UAV with respect to the Earth in $\mathcal{F}^b$ such that:

$$\boldsymbol{a}^b_{BE} = \begin{pmatrix} a_x \\ a_y \\ a_z \end{pmatrix}; \boldsymbol{v}^b_{BE} = \begin{pmatrix} u \\ v \\ w \end{pmatrix}; \boldsymbol{\omega}^b_{BE} = \begin{pmatrix} p \\ q \\ r \end{pmatrix}. \quad (1)$$

Based on $\boldsymbol{v}^b_{BE}$, the definitions of the airspeed V_a, the angle of attack α, and the sideslip angle β are given as:

$$V_a = \sqrt{u^2 + v^2 + w^2}; \quad (2)$$

$$\alpha = \tan^{-1}\left(\frac{w}{u}\right); \quad (3)$$

$$\beta = \sin^{-1}\left(\frac{v}{V_a}\right). \quad (4)$$

Moreover, the Newton-Euler laws of motion write:

$$\dot{\boldsymbol{v}}^b_{BE} = \frac{\boldsymbol{F}^b}{m} - \boldsymbol{\omega}^b_{BE} \times \boldsymbol{v}^b_{BE}; \quad (5)$$

$$\dot{\boldsymbol{\omega}}^b_{BE} = \boldsymbol{I}^{-1}(\boldsymbol{M}^b - \boldsymbol{\omega}^b_{BE} \times \boldsymbol{I}\boldsymbol{\omega}^b_{BE}), \quad (6)$$

where $\boldsymbol{F}^b$ are the resultant forces, $\boldsymbol{M}^b$ the resultant moments in the body frame, and $\boldsymbol{I}$ the inertia matrix.

This set of equations defines the translational (5) and rotational dynamics (6), respectively. However, in the identification process, an alternative formulation of translational dynamics is preferred, valid under the assumption of no wind. It is obtained by isolating u, v, w in Equations (2–4), and get $\dot{u}$, $\dot{v}$, $\dot{w}$ after differentiation with respect to time. These components are substituted into Equation (5). The formulation is given as in [5]:

$$\begin{aligned}
\dot{V}_a &= \frac{1}{m}(\cos\alpha\cos\beta\, X + \sin\beta Y \\
&\quad + \sin\alpha\cos\beta\, Z); && (7)\\
\dot{\alpha} &= -\tan\beta\cos\alpha\, p + q - \tan\beta\sin\alpha\, r \\
&\quad + \frac{1}{mV_a}\left(-\frac{\sin\alpha}{\cos\beta}X + \frac{\cos\alpha}{\cos\beta}Z\right); && (8)\\
\dot{\beta} &= \sin\alpha\, p - \cos\alpha\, r + \frac{1}{mV_a}(-\cos\alpha\sin\beta\, X \\
&\quad + \cos\beta\, Y - \sin\alpha\sin\beta\, Z), && (9)
\end{aligned}$$

where $(X, Y, Z)^T$ are the coordinates of the resultant force $\boldsymbol{F}^b$ along the body frame axes.

3.3 Actuators

1. *Servomotors:* They actuate the elevons and rudder of the UAV. Their dynamics are not negligible, hence, each is modeled by a first-order transfer function with time constant τ, along with a pure time delay named τ_a.

2. *Motor-Propeller Model:* The propulsion chain is composed by the ESC, the motor and the propeller. The ESC acts as a switching voltage stage that converts the throttle command δ_t into an effective motor input voltage u_m as:

$$u_m = V_{bat}\delta_t, \tag{10}$$

where V_{bat} is the battery voltage. The transfer from u_m to the motor angular speed Ω is nonlinear and modeled as a Hammerstein model: at the input, a polynomial function captures the static nonlinearity of the ESC-motor pair:

$$\Omega_{ss} = a_{esc}u_m^2 + b_{esc}u_m, \tag{11}$$

where Ω_{ss} is the steady-state motor speed. At the output, the dynamics are modeled as a second-order transfer function as:

$$\frac{\Omega}{\Omega_{ss}} = \frac{1}{1 + \frac{2\zeta}{\omega_0}s + \frac{1}{\omega_0^2}s^2}, \tag{12}$$

where ω_0 is the motor natural frequency, ζ its damping ratio and s is the Laplace variable.

3.4 Forces and Moments

1. *Gravitational Force:* In the inertial frame, it can be expressed by:

$$\boldsymbol{F}_g^i = \begin{pmatrix} 0 \\ 0 \\ mg \end{pmatrix}, \tag{13}$$

where g is the acceleration due to gravity.

2. *Aerodynamic Forces and Moments:* Aerodynamic forces are expressed as follows in the wind frame:

$$\boldsymbol{F}_{aero}^w = -\frac{1}{2}\rho V_a^2 S \begin{pmatrix} C_D \\ C_Y \\ C_L \end{pmatrix}, \tag{14}$$

where ρ is the air density, S the reference surface, $C_{\{D,Y,L\}}$ the drag, side-force and lift coefficients, respectively. Aerodynamic moments are expressed as follows in the wind or body frame:

$$\boldsymbol{M}_{aero}^b = \boldsymbol{M}_{aero}^w = \frac{1}{2}\rho V_a^2 S \begin{pmatrix} bC_l \\ cC_m \\ bC_n \end{pmatrix}, \tag{15}$$

where b is the wingspan of the UAV, c its wing chord, $C_{\{l,m,n\}}$ the rolling, pitching and yawing moment coefficients, respectively.

The air density ρ is given by an implementation of the ISA atmosphere model, and computed from the altitude of the vehicle.

Then, the following decomposition of the aerodynamic coefficients is used, respectively for the longitudinal and lateral models:

$$\begin{pmatrix} C_D \\ C_L \\ C_m \end{pmatrix} = \begin{pmatrix} C_{D0} \\ C_{L0} \\ C_{m0} \end{pmatrix} + \begin{pmatrix} C_{D\alpha^2}\alpha & \frac{c}{2V_a}C_{Dq} \\ C_{L\alpha} & \frac{c}{2V_a}C_{Lq} \\ C_{m\alpha} & \frac{c}{2V_a}C_{mq} \end{pmatrix}\begin{pmatrix} \alpha \\ q \end{pmatrix} + \begin{pmatrix} C_{D\delta_e} \\ C_{L\delta_e} \\ C_{m\delta_e} \end{pmatrix}\delta_e; \tag{16}$$

$$\begin{aligned}
\begin{pmatrix} C_Y \\ C_l \\ C_n \end{pmatrix} &= \begin{pmatrix} 0 \\ C_{l0} \\ C_{n0} \end{pmatrix} \\
&\quad + \begin{pmatrix} C_{Y\beta} & \frac{b}{2V_a}C_{Yp} & \frac{b}{2V_a}C_{Yr} \\ C_{l\beta} & \frac{b}{2V_a}C_{lp} & \frac{b}{2V_a}C_{lr} \\ C_{n\beta} & \frac{b}{2V_a}C_{np} & \frac{b}{2V_a}C_{nr} \end{pmatrix}\begin{pmatrix} \beta \\ p \\ r \end{pmatrix} \\
&\quad + \begin{pmatrix} C_{Y\delta_a} & C_{Y\delta_r} \\ C_{l\delta_a} & C_{l\delta_r} \\ C_{n\delta_a} & C_{n\delta_r} \end{pmatrix}\begin{pmatrix} \delta_a \\ \delta_r \end{pmatrix}, && (17)
\end{aligned}$$

where $\delta_{\{a,e,r\}}$ are the roll, pitch and yaw control inputs, respectively.

3. *Propulsion Forces and Moments:* In the body frame, propulsion forces can be expressed using standard model from blade theory by:

$$\boldsymbol{F}^b_{prop} = \begin{pmatrix} \rho D_p^4 (\frac{\Omega}{2\pi})^2 C_T \\ 0 \\ 0 \end{pmatrix}, \tag{18}$$

where D_p is the diameter of the propeller. Besides, propulsion moments are defined as follows in the body frame:

$$\boldsymbol{M}^b_{prop} = \begin{pmatrix} \rho D_p^5 (\frac{\Omega}{2\pi})^2 C_Q \\ 0 \\ 0 \end{pmatrix}. \tag{19}$$

4. *Gyroscopic and Reaction Wheel Effect:* The gyroscopic moment due to rotation of the motor can be expressed as follows in the body frame:

$$\boldsymbol{M}^b_{gyro} = I_{pr} \begin{pmatrix} -\dot{\Omega} \\ -\Omega r \\ \Omega q \end{pmatrix}, \tag{20}$$

where I_{pr} is the moment of inertia of the rotor and the propeller.

4 NONLINEAR SYSTEM IDENTIFICATION

Based on the nonlinear model of the system derived in Section 3 and on data collected during flight tests, the overall goal of the method is to estimate the aerodynamic coefficients appearing in Equations (16) and (17). Previous tests have shown that some coefficients are very small and have a negligible effect on the outputs, in particular C_{L_q}, C_{n_0} and the coupling coefficients $C_{Y_{p,r}}$, C_{l_r}, C_{m_p} and C_{n_p}. Therefore, they are fixed to zero and will not be estimated in this paper. Besides, the available data are insufficient to estimate the second-order term $C_{D_{\alpha^2}}$, which can be obtained through CFD calculations.

4.1 Motor-Propeller Model Coefficients Estimation

The parameters of Equations (11–12) were determined beforehand using a dedicated test bench to measure the motor speed and supply voltage during testing. Parameters a_{ESC} and b_{ESC} were first identified from the steady-state function $\Omega_{ss}(u_m)$. Then, parameters ζ and ω_0 were estimated to fit step variations. The propeller coefficients C_T and C_Q were estimated from propeller performance curves given by the manufacturer [1] [2]. While the servomotors time constant τ was computed from measurements made on a dedicated test bench, the delay τ_a was estimated directly from input-output flight data, thus taking into account not only the servomotor delay but also additional delays in the loop. All the system parameters are listed in Table 2.

[1]https://m-selig.ae.illinois.edu/props/propDB.html
[2]https://www.apcprop.com/technical-information/performance-data

Sym.	Name	Value
m	Mass	$0.750\,\mathrm{kg}$
x_{CG}	Position of CG /nose	$-0.21\,\mathrm{m}$
I_{11}	Moment of inertia (x-axis)	$0.009\,09\,\mathrm{kg\,m^2}$
I_{22}	Moment of inertia (y-axis)	$0.007\,29\,\mathrm{kg\,m^2}$
I_{33}	Moment of inertia (z-axis)	$0.0157\,\mathrm{kg\,m^2}$
I_{13}	x-z product of inertia	$-0.000\,458\,\mathrm{kg\,m^2}$
b	Wingspan	$0.80\,\mathrm{m}$
c	Wing chord	$0.25\,\mathrm{m}$
S	Reference surface	$0.20\,\mathrm{m^2}$
V_{bat}	Battery voltage	$16.0\,\mathrm{V}$
τ	Servos time constant	$0.013\,\mathrm{s}$
τ_a	Servos actuator delay	$0.033\,\mathrm{s}$
a_{esc}	Quadratic ESC coef.	$-14.35\,\mathrm{rad\,s^{-1}\,V^{-2}}$
b_{esc}	Linear ESC coef.	$287.85\,\mathrm{rad\,s^{-1}\,V^{-1}}$
ω_0	Motor angular freq.	$17.94\,\mathrm{rad\,s^{-1}}$
ζ	Motor damping ratio	1.86
C_T	Thrust coef.	0.146
C_Q	Torque coef.	0.066

Table 2: Predetermined system parameters

4.2 Excitation Trajectory

Excitation signals are applied to each axis independently and are superimposed to pilot commands. By this mean, the pilot can correct the trajectory of the UAV if needed, in order to stay close to level-flight in straight line. Pilot's corrections are kept as small as possible. Several excitation signals could be used [6, 8]. In this work, they consist in 3-level step inputs, which are rather straightforward to implement.

Both amplitude and frequency of the multistep have been adjusted empirically during flight via the remote control. The amplitude has been tuned to ensure sufficient signal-to-noise ratio while keeping deviations from the nominal trajectory within acceptable limits. Likewise, the frequency has been adapted to the system dynamics so that quasi-steady-state conditions are reached after each excitation step.

Control input signals, as well as the measured angular velocities, are shown in Figure 2 for both roll and pitch axes. The yaw dynamics have not been considered in this study and no excitation is then provided on this axis.

Vectors of measured values are extracted from PX4 flight logs and uniformly resampled onto a common time base. Quaternions from the "vehicle-attitude" topic are used to compute the rotation matrix from the local to the body frame, as well as the Euler angles. Linear velocities and positions come from the "vehicle-local-position" topic, while angular rates come from "vehicle-angular-velocity". Accelerometer measurements (specific force) come from "vehicle-acceleration" and are used to compute body inertial accelerations by adding gravity. Measurements of V_a, α and β are computed from definitions (2–4). Control inputs are taken directly from the "torque-setpoint" and "thrust-setpoint" topics.

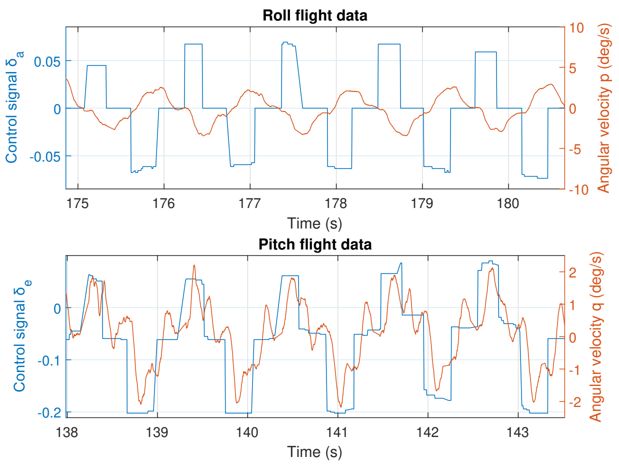

Figure 2: Roll and pitch angular velocities with control input signals.

4.3 *Aerodynamic Coefficient Estimation Method*

Experience shows that attempting to estimate the complete set of aerodynamic coefficient derivatives described in Equations (16) and (17) in a single optimization problem leads to convergence stalls or drift towards non-physical values (due to local minima, compensations between parameters, strong dependence on the initial guess). To reduce the complexity, the coefficients are estimated in seven stages, each stage involving estimation of a subset of one to four coefficients only, and the selection of a single output, as shown in Table 3. This approach eliminates strong parameter interdependence and yields robust convergence to physically meaningful values.

At each stage, the considered aerodynamic coefficients are estimated with the output-error method [5, 6]. The channel-wise accumulated squared errors in angular rate ($\boldsymbol{\epsilon}_\omega$) and acceleration ($\boldsymbol{\epsilon}_a$) are defined as:

$$\boldsymbol{\epsilon}_\omega(j) = \sum_i \left(\boldsymbol{\omega}^b_{BE,s}(i,j) - \boldsymbol{\omega}^b_{BE,m}(i,j)\right)^2; \qquad (21)$$

$$\boldsymbol{\epsilon}_a(j) = \sum_i \left(\boldsymbol{a}^b_{BE,s}(i,j) - \boldsymbol{a}^b_{BE,m}(i,j)\right)^2, \qquad (22)$$

where $i = 1, \ldots, N$ is the sample time index, $j = 1,2,3$ the body axes, and where "s", "m" indicate simulated and measured outputs, respectively. These notations will be kept in the next paragraphs. Vectors $\boldsymbol{\epsilon}_\omega$ and $\boldsymbol{\epsilon}_a$ are three-dimensional.

The scalar criterion J_k to be minimized by the optimization procedure is the weighted least-squares error computed as the squared differences between simulated and measured flight data as follows:

$$J_k = \boldsymbol{w}_k \begin{bmatrix} \boldsymbol{\epsilon}_\omega \\ \boldsymbol{\epsilon}_a \end{bmatrix}. \qquad (23)$$

The weight vector $\boldsymbol{w}_k$ allows selective activation or scaling of each channel, where $k = 1, \ldots, 7$ is the coefficient subset index (for example, $\boldsymbol{w}_k = [0,1,0,0,0,1]$ includes only pitch rate and z-axis acceleration errors in the cost).

k	**Coefs.**	**Submodel eq.**	**Meas. inputs**	**Weight $\boldsymbol{w}_k$**
1	C_{L_0} C_{L_α} $C_{L_{\delta_e}}$	α dynamics from (8), (2)	$\delta_{\{a,e,r,t\}}$ p_m, q_m, r_m u_m, v_m, w_m	$[0,0,0,\ldots$ $0,0,1]$
2	C_{D_0}	α dynamics from (8), (2)	$\delta_{\{a,e,r,t\}}$ p_m, q_m, r_m u_m, v_m, w_m	$[0,0,0,\ldots$ $1,0,0]$
3	C_{Y_β} $C_{Y_{\delta_a}}$ $C_{Y_{\delta_r}}$	α, β from (8)-(9) and (2)	$\delta_{\{a,e,r,t\}}$ p_m, q_m, r_m u_m, v_m, w_m	$[0,0,0,\ldots$ $0,1,0]$
4	C_{m_0} C_{m_α} $C_{m_{\delta_e}}$ C_{m_q}	q from (6) V_a, α from (7)-(8)	$\delta_{\{a,e,r,t\}}$ p_m, q_m, r_m	$[0,1,0,\ldots$ $0,0,0]$
5	C_{l_0} C_{l_β} C_{l_p} $C_{l_{\delta_a}}$ $C_{l_{\delta_r}}$	p from (6) V_a, α, β from (7)-(9)	$\delta_{\{a,e,r,t\}}$ q_m, r_m	$[1,0,0,\ldots$ $0,0,0]$
6	C_{D_0} C_{D_q} $C_{D_{\delta_e}}$	V_a, α from (7)-(8)	$\delta_{\{a,e,r,t\}}$ p_m, q_m, r_m	$[0,0,0,\ldots$ $1,0,0]$
7	C_{n_β} C_{n_r} $C_{n_{\delta_a}}$	r from (6) V_a, α, β from (7)-(9)	$\delta_{\{a,e,r,t\}}$ p_m, q_m	$[0,0,1,\ldots$ $0,0,0]$

Table 3: Aerodynamic coefficient estimation

Each line k of Table 3 defines an optimization problem: it specifies the subset of coefficients to be estimated (second column), the associated sub-model equations (third column), the measurements used as inputs (fourth column), and the weighting vector $\boldsymbol{w}_k$ employed in the cost function J_k (last column).

Linear and angular velocities can be obtained either directly from measurements or from the translational and rotational dynamics. Accordingly, depending on the subset of coefficients to be estimated (i.e. the stage k in Table 3), V_a, α, β are computed either from definitions (2–4) using the measured velocity $\boldsymbol{v}^b_{BE,m}$, or by solving the translational dynamics differential equations (7–9). Similarly, the angular velocity is obtained either from measurements $\boldsymbol{\omega}^b_{BE,m}$, or from rotational dynamics in Equation (6). The chosen set of equations is indicated in the third column of Table 3.

4.4 *Aerodynamic Coefficient Estimated Values*

To estimate the aerodynamic coefficients, the output-error method is applied using the Nelder-Mead simplex algorithm [17]. The coefficients obtained for the tail-sitter UAV with the identification approach are given in Table 4, compared to CFD values obtained from steady RANS simulations using the DLR TAU-Code [18]. Since no yaw inputs were used, $C_{Y_{\delta_r}}$, $C_{l_{\delta_r}}$ and $C_{n_{\delta_r}}$ are set to zero. Other $C_{n.}$ coefficients associated with the yaw axis are still estimated.

Coefs.	Estimated	CFD	Abs. err.	Rel. err.
C_{L_0}	0.005	0.026	0.021	80.8 %
C_{L_α}	1.186	3.449	2.263	65.6 %
$C_{L_{\delta_e}}$	0.350	/	/	/
C_{D_0}	0.125	0.021	0.104	495.2 %
C_{D_q}	0.000	/	/	/
$C_{D_{\delta_e}}$	0.001	/	/	/
C_{Y_β}	-0.006	-0.929	0.923	99.4 %
$C_{Y_{\delta_a}}$	0.005	/	/	/
C_{l_0}	-0.004	0.000	/	/
$C_{l\beta}$	-0.005	-0.003	0.002	66.7 %
C_{l_p}	-0.091	/	/	/
$C_{l\delta_a}$	-0.054	/	/	/
C_{m_0}	0.036	0.000	/	/
C_{m_α}	-0.193	-0.196	0.003	1.5 %
$C_{m_{\delta_e}}$	0.243	/	/	/
C_{m_q}	-3.427	/	/	/
C_{n_β}	0.100	0.169	0.069	40.8 %
C_{n_r}	-0.085	/	/	/
$C_{n_{\delta_a}}$	0.026	/	/	/

Table 4: Estimated aerodynamic coefficients compared to CFD results

The estimated values are overall consistent with the CFD predictions, and the discrepancies can be traced to modeling assumptions. First, the CFD simulations are performed on an ideal airfoil geometry: surface roughness, wing-mounted hardware (Pitot tube, protruding batteries, cables...) and, most importantly, the rotor disk located in the middle of the wing is not taken into account. Consequently, the lift-curve slope estimated from flight data, $C_{L_\alpha} = 1.186$ is significantly lower than the CFD value of 3.449. The same reasoning explains why the zero-lift drag coefficient exceeds the CFD result ($C_{D_0} = 0.125$ vs. 0.021 with the CFD); the real aircraft experiences more drag than the ideal laminar-flow profile assumed in CFD.

Coefficient C_{Y_β} also shows a large discrepancy of -0.006 vs. -0.929. This is due to the lack of yaw excitation data in the identification dataset, leading to low observability of the corresponding dynamics. By contrast, the static pitch-stability derivative $C_{m_\alpha} = -0.193$ matches the CFD value of -0.196 very closely and the values for the yaw-stability derivative C_{n_β} are close as well, confirming that the identification method captures these important stability terms with high fidelity. The non-zero value of C_{l_0} might traduce an asymmetry in the wing or elevons structure. Finally, it should be noted that the control-derivative coefficients (e.g. $C_{L_{\delta_e}}$ and $C_{m_{\delta_e}}$) and the dynamic coefficients (e.g. C_{m_q} and C_{l_p}) are notoriously difficult to obtain from CFD: the former require a large number of simulations for each control-surface deflection, while the latter demand complex coupling between CFD and dynamics. System identification, on the other hand, yields an estimate for these values.

The fitting results of the model to the flight data are shown in Figures 3 and 4. Two datasets collected during two different flights are used, one for identification and one for validation. The fitting percentage to evaluate the accuracy of the identification process is computed from a normalized root-mean-squared error, and given by:

$$f_{\%} = 100 \left(1 - \frac{\|\boldsymbol{y}_s - \boldsymbol{y}_m\|}{\|\boldsymbol{y}_m - \bar{\boldsymbol{y}}_m\|}\right), \tag{24}$$

where $\boldsymbol{y}_s$ is the simulated output vector, $\boldsymbol{y}_m$ the measured output vector, $\bar{\boldsymbol{y}}_m$ the sample mean of $\boldsymbol{y}_m$, and $\|\cdot\|$ denotes the Euclidean (2-)norm.

The fitting values for both identification and validation datasets are satisfactory. Indeed, on both datasets, the roll angular velocity p has a fit around $50\,\%$, and the acceleration a_y fit is higher than $80\,\%$. Moreover, pitch angular velocity q and acceleration a_z also have a fit between $40\,\%$ and $60\,\%$ on the identification dataset. On the validation dataset, the fits are lower for the latter axes, which can be explained by visible offsets. These can be attributed to differences in mass distribution between the tested configuration and the nominal model, as well as to trim changes commanded by the pilot via the remote control during flight. These effects modify the effective trim state and control biases seen in the measurements, but are not fully captured by the nominal aerodynamic model, which explains the observed offsets. Relatively low fit values on acceleration a_x is likely caused by the differing conditions between the motor-propeller test bench setup and real-world flight, and by the presence of wind during the experiments. Finally, the low yaw-rate fits (around 13%) are expected, because no yaw excitation have been used in this study.

Figures 3 and 4 also show α and β as predicted by the model, based on translational dynamics (8-9). On both datasets, β remains almost zero, which shows very low sideslip. In addition, α stays between $0°$ and $15°$, which is realistic in terms of angle of attack variations. As an additional validation, the model's predictions for the airspeed V_a agree well with the measurements on both identification (Figure 3) and validation (Figure 4) datasets, even though V_a was not used during the identification process.

5 CONCLUSION

This paper presents a generic nonlinear system identification method and its application to aerodynamic coefficient estimation of a tail-sitter VTOL drone in fixed-wing mode. The approach only needs a few dozen seconds of flight data, which avoids performing numerous measurement campaigns. The aerodynamic coefficients are estimated in stages using the output-error method, which eliminates strong parameter

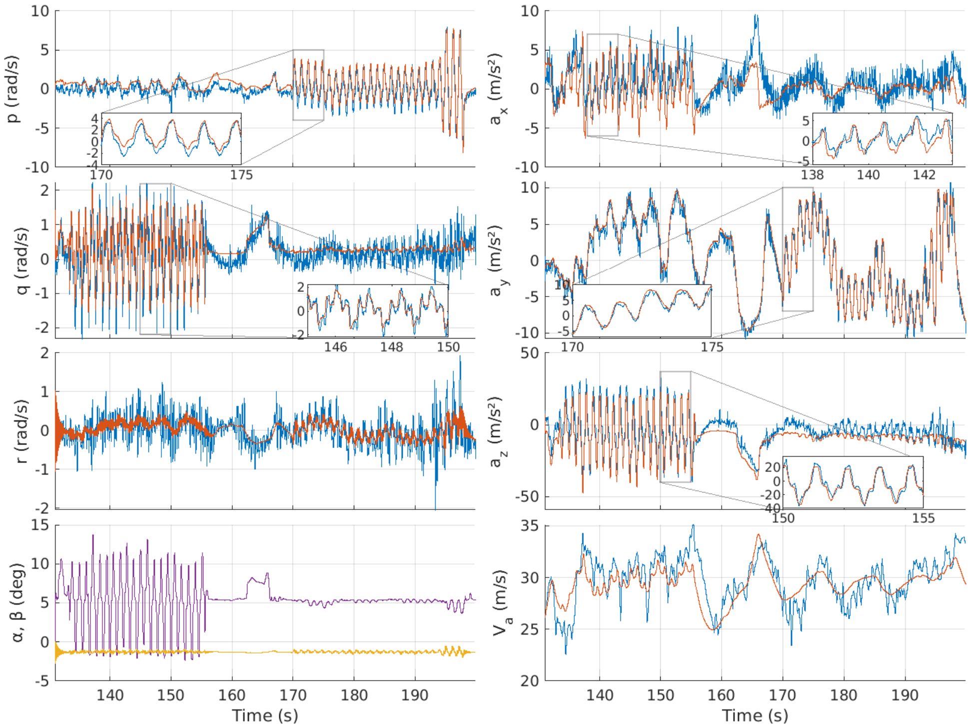

Figure 3: Identification results, with flight data in blue, model data in orange, α in purple and β in yellow. The fitting values are the following: $f_p = 46.5\%$, $f_q = 41.4\%$, $f_r = 13.3\%$, $f_{a_x} = 4.7\%$, $f_{a_y} = 82.4\%$, $f_{a_z} = 51.2\%$.

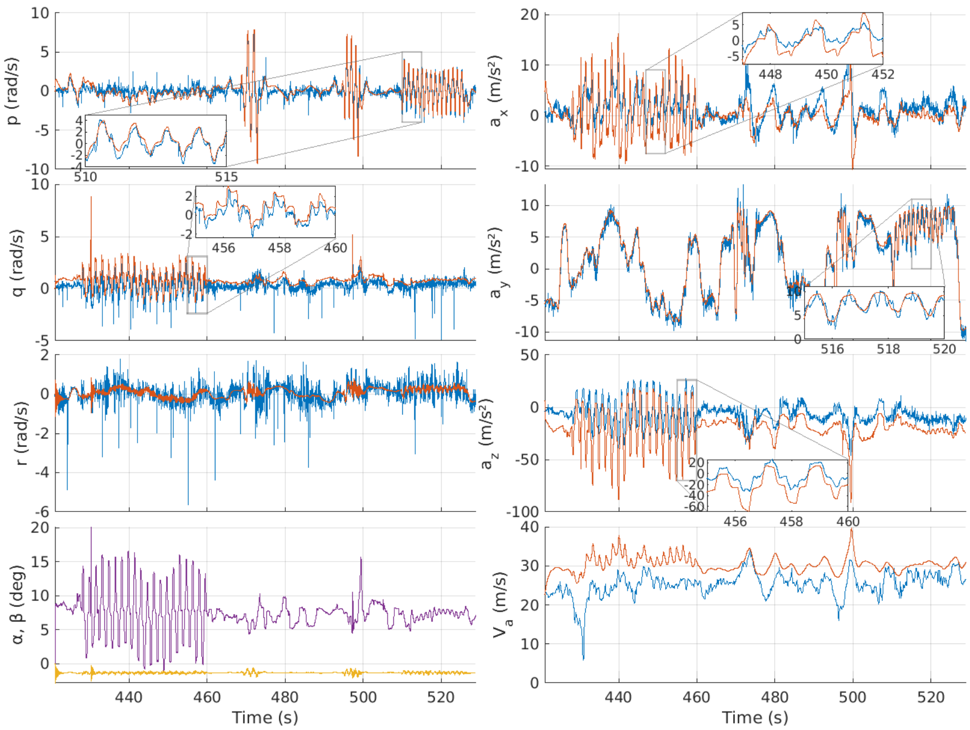

Figure 4: Validation results, with flight data in blue, model data in orange, α in purple and β in yellow. The fitting values are the following: $f_p = 54.1\%$, $f_q = -0.5\%$, $f_r = 13.6\%$, $f_{a_x} = -4.1\%$, $f_{a_y} = 84.5\%$, $f_{a_z} = -35.1\%$.

interdependence and yields robust convergence to physically meaningful values. A limitation of the method is its sensitivity to data biases, due e.g. to miscalibrated accelerations and presence of wind during tests. Nevertheless, such biases mostly affect offset coefficients which have no impact on the linearized dynamics used for control design. Overall, the results are consistent with values predicted from CFD simulations, and satisfactory model fits to independent flight test data validate the entire methodology. Future work will include assessing the robustness of the methodology using simulated data. Besides, coefficients validity will be extended from fixed-wing flight to hover flight through the use of high-angle-of-attack analytical models.

REFERENCES

[1] Guillaume JJ Ducard and Mike Allenspach. Review of designs and flight control techniques of hybrid and convertible VTOL UAVs. *Aerospace Science and Technology*, 118:107035, 2021.

[2] Adnan S Saeed, Ahmad B Younes, Chenxiao Cai, and Guowei Cai. A survey of hybrid unmanned aerial vehicles. *Progress in Aerospace Sciences*, 98:91–105, 2018.

[3] Michael Selig. Modeling full-envelope aerodynamics of small UAVs in realtime. In *AIAA Atmospheric Flight Mechanics Conference*, page 7635, 2010.

[4] Ziqing Ma. *Design and Control of a Tilt-Rotor Tailsitter Aircraft*. PhD thesis, TU Delft, 2026.

[5] Eugene A Morelli and Vladislav Klein. *Aircraft System Identification: Theory and Practice*, volume 2. Sunflyte Enterprises Williamsburg, VA, 2016.

[6] Ravindra V Jategaonkar. *Flight Vehicle System Identification: A Time Domain Methodology*. American Institute of Aeronautics and Astronautics, 2006.

[7] Nathan V Hoffer, Calvin Coopmans, Austin M Jensen, and YangQuan Chen. A survey and categorization of small low-cost unmanned aerial vehicle system identification. *Journal of Intelligent & Robotic Systems*, 74(1):129–145, 2014.

[8] Benjamin M Simmons, James L Gresham, and Craig A Woolsey. Flight-test system identification techniques and applications for small, low-cost, fixed-wing aircraft. *Journal of Aircraft*, 60(5):1503–1521, 2023.

[9] Vishwas R Puttige and Sreenatha G Anavatti. Real-time system identification of unmanned aerial vehicles: A multi-network approach. *Journal of Computers*, 3(7):31–38, 2008.

[10] Andrei Dorobantu, Austin Murch, Bérénice Mettler, and Gary Balas. System identification for small, low-cost, fixed-wing unmanned aircraft. *Journal of Aircraft*, 50(4):1117–1130, 2013.

[11] Nirmal Kumar, Subrahmanyam Saderla, and Y Kim. Parametric model identification of delta wing UAVs using filter error method augmented with particle swarm optimisation. *The Aeronautical Journal*, 127(1312):982–1008, 2023.

[12] Weifeng Zhou, Shengyang Chen, Ching-Wei Chang, Chih-Yung Wen, Chih-Keng Chen, and Boyang Li. System identification and control for a tail-sitter unmanned aerial vehicle in the cruise flight. *IEEE Access : Practical Innovations, Open Solutions*, 8:218348–218359, 2020.

[13] Hosun Lee, Jayden D Lee, and Hyochoong Bang. Aerodynamic model identification of a VTOL tailsitter UAV using sparse identification of nonlinear dynamics. In *ICAS Proceedings*, 2024.

[14] Carl Olsson, Sebastian L Verling, Thomas Stastny, and Roland Siegwart. Full envelope system identification of a VTOL tailsitter UAV. In *AIAA Scitech 2021 Forum*, page 1054, 2021.

[15] Lorenz Meier, Dominik Honegger, and Marc Pollefeys. PX4: A node-based multithreaded open source robotics framework for deeply embedded platforms. In *IEEE International Conference on Robotics and Automation*, pages 6235–6240, 2015.

[16] Randal W Beard and Timothy W McLain. *Small Unmanned Aircraft: Theory and Practice*. Princeton University Press, 2012.

[17] Jeffrey C Lagarias, James A Reeds, Margaret H Wright, and Paul E Wright. Convergence properties of the Nelder–Mead simplex method in low dimensions. *SIAM Journal on Optimization*, 9(1):112–147, 1998.

[18] Dieter Schwamborn, Thomas Gerhold, and Ralf Heinrich. The DLR TAU-code: Recent applications in research and industry. In *ECCOMAS CFD: Proceedings of the European Conference on Computational Fluid Dynamics*, Egmond aan Zee, the Netherlands, 2006.